A Modified PEG-Fe$_3$O$_4$ Magnetic Nanoparticles Conjugated with D(+) Glucosamine (DG): MRI Contrast Agent

Ali Hossein Rezayan[1] · Somayyeh Kheirjou[2] · Maryam Edrisi[1] · Mehdi Shafiee Ardestani[3] · Hale Alvandi[1]

Abstract

Molecular imaging (MI) can provide not only structural images utilizing temporal imaging techniques, but also functional and molecular data using a variety of newly developed imaging techniques. Nanotechnology's application in MI has commanded a lot of attention in recent decades, and it has provided tremendous potential for imaging living subjects. In this study, D-glucosamine conjugated functionalized magnetic iron oxide nanoparticles (Fe$_3$O$_4$-PEG-DG NPs) were prepared and studied as magnetic resonance imaging (MRI) contrast agents. To evaluate their distribution, single-photon emission computed tomography (SPECT) is performed. Fe$_3$O$_4$ NPs are made using a well-known co-precipitation process and subsequently coated with PEG 3450. Fe$_3$O$_4$-PEG NPs were coupled to D-glucosamine to specifically target breast cancer cells. The resulted modified NPs were characterized by XRD, VSM, FESEM, and FTIR analysis. Moreover, the prepared contrast agent was studied through different biological assays, including MTT assay, T2-weighted in vitro MRI, and biodistribution analysis. Fe$_3$O$_4$-PEG-DG NPs particle size and zeta potential were 98 nm and − 7.5 mV, respectively. Cytotoxicity was performed on normal human kidney (HEK-293) cells due to their high sensitivity to MRI contrast agents; Fe$_3$O$_4$-PEG-DG NPs had a very slight toxicity effect on these cells and cell viability was more than 75%. MRI images of Fe$_3$O$_4$-PEG-DG NPs show these NPs significantly reduce the signal intensity and increase the contrast. Animal studies show Fe$_3$O$_4$-PEG-DG NPs tend to be highly sensitive to tissues with active metabolisms, such as the gastrointestinal tract. These nanoparticles can be a suitable MRI contrast agent and improve the quality of MRI images.

Keywords Magnetic resonance imaging (MRI) · D(+)Glucosamine (DG) · Fe$_3$O$_4$ NPs · Polyethylene glycol (PEG) · Contrast agent

1 Introduction

Cancer is a difficult disease that affects millions of people around the world. Breast cancer has been identified as one of the most common forms among its many varieties. Despite the fact that mammography and sidelong therapies have reduced breast cancer mortality rates, there is an increasing desire for innovative therapy and diagnosis approaches.

Breast cancer is treated primarily with surgery, followed by adjuvant chemotherapy or radiotherapy. Although this method has been beneficial in the majority of patients, it should be noted that it damages both normal and unhealthy tissues and organs at the same time [1–4]. As a result, a strategy that involves direct targeting of cancer cells by particular targeting agents that bind to cancer cells selectively provides an alternative to regular chemotherapy. Carbohydrates, lectins, peptides, and antibodies are just a few of the ligands that have been found and used to directly target cancer cells. Each of these conjugating ligands, which are utilized to target cells in a specific site of action for diagnosis or treatment, has its own set of advantages and disadvantages [3, 5–10].

There are different diagnosis techniques, such as single-photon emission computed tomography (SPECT), X-ray computed tomography (CT), ultrasound, positron emission tomography (PET), and magnetic resonance imaging (MRI).

✉ Ali Hossein Rezayan
ahrezayan@ut.ac.ir

1 Division of Nanobiotechnology, Department of Life Science Engineering, Faculty of New Sciences and Technologies, University of Tehran, P.O. Box 14395-1561, Tehran, Iran

2 Department of Chemistry, Sharif University of Technology, Tehran, Iran

3 Department of Pharmacy, Tehran University of Medical Sciences, Tehran, Iran

In comparison, MRI is widely used since other molecular imaging techniques have high sensitivity but low spatial resolution, making them ineffective in properly identifying the body's anatomical parts. Furthermore, they use ionizing radiation; however, because MRI has a high spatial resolution, it does not require ionizing radiation; nonetheless, because it has a poor sensitivity by design, contrast agents should be employed to boost sensitivity. MRI technology gives excellent precision from human organs and is widely employed around the world today [11–21].

There are three basic types of MRI scan, including the longitudinal relaxation time (T1)-weighted, (T2)-weighted, short T1 inversion recovery (STIR), and fluid attenuation inversion recovery (FLAIR). The MRI technique's most significant challenge is its poor signal intensity and diagnosis sensitivity. Using contrast agents is one way to get around this problem. Contrast agents, such as magnetic metal ions, are now used in over half of all MRI scans to improve diagnosis sensitivity [11, 22]. To reduce side effects, the T1 contrast agent is commonly chelated transitional metal ion or lanthanide [23–27], while the T2 contrast agent is usually superparamagnetic nanoparticles (NPs) with coating layers [28].

Fe_3O_4 NPs have been widely studied and drawn attention owing to their particular features, such as their environmentally benign nature, stability, secure storage, and operation [18, 29–32]. They are potential materials for labeling cells and biomolecules, bio separation, hyperthermia, drug administration, and MRI contrast enrichment because to their strong magnetic characteristics [31, 33, 34]. Many scientists have recently become interested in the biomedical applications of NPs, particularly Fe_3O_4. For instance, Gupta has done several studies on the application of Fe_3O_4 NPs in biomedicine. Also, Xie et al. have reported the application of superparamagnetic Fe_3O_4 NPs as negative MRI contrast agents [29–31].

The higher permeability and longevity of NPs explain their appropriateness for use as targeted carriers and their substantial accumulation in tumor tissues. Furthermore, NPs have a longer retention duration in blood medium, which causes a rise in the concentration of the associated drug in the target tissue, a phenomenon known as the enhanced permeability retention (EPR) effect [35]. To achieve these virtues, NPs must be coated with different materials and then attached to the target molecule.

Breast cancer growth is influenced by a variety of circumstances, and various molecules have been identified as breast tumor indicators. Glucose analogs are a very successful agent in the detection and treatment of metastatic breast cancer. In the absence of oxygen, cancer cells prefer the glycolytic pathway for glucose metabolism [36]. In contrast to oxidative phosphorylation, glycolysis has a lower efficiency in ATP production, called the Warburg effect. Glycolic metabolism requires a significant amount of glucose. Glucose uptake in breast cancer cells augments by increasing the glucose transporter (GLUT) expression, mainly GLUT1, that carries glucose into the cells [37]. This is the basis for clinical imaging and tumor staging via PET. [18F] Fluoro-2-deoxy-d-glucose [(18F) FDG] is a glucose analogous used in PET; however, it has a small amount of radiation emission and a short half-life.

These molecules are absorbed by glucose transporters, introduced into the tumor, and kept there by phosphorylation as a diagnostic chemical. This glucose analogous uses tagged markers to offer a quantitative measurement of glycolysis that can be utilized to detect cancers in their early stages. Glucose analogs are transported by GLUT1-4 transducers and have a similar structure to D-glucose. Increasing metabolic requirements in tumor cells increase the withdrawal of these analogs, which block the activity of hexose phosphate isomerases that converts glucose 6-phosphate into 1–6-di-phosphate. This enzyme blockage results in a defect in cancer cell's glycolysis cycle, leading to reduced metabolism. Also, with a decrease in cancer cells' metabolism, the secretion of this enzyme probably curtails, which gives rise to slow the metastasis [37].

In continuation of our interest in the synthesis of nanomaterials and investigation of their application in diagnosis, treatment, and environmental remediation [38–42], in this study, a new MRI contrast agent, i.e., PEGylated D-glucosamine functionalized magnetic Fe_3O_4 NPs (Fe_3O_4-PEG-DG), was prepared and investigated. This contrast agent efficiency was evaluated by changing the imaging signal using in vitro MRI, and the SPECT assessed its biological distribution in vivo. Also, the biological activity of Fe_3O_4-PEG-DG NPs was analyzed via in vitro cytotoxicity analysis.

2 Experimental Section

2.1 Materials

All reagents and solvents were purchased from Merck (Germany) and used without more purification. All the used containers and equipment were first washed with distilled water, alcohol, deionized water, and acetone to prevent the introduction of impurities.

2.2 Synthesis of Fe_3O_4-PEG-DG NPs

Common co-precipitation approach was utilized for the synthesis of Fe_3O_4 NPs. The repute of this method is due to its ease of use and high efficiency. In addition, by dominating the synthesis parameters, such as pH, the particles size can be partially controlled. However, beyond its benefits, it has some disadvantageous too. For example, the particle size

in this method is not uniform. So, in this study, ultrasonic waves were used to narrow the size distribution. In order to prevent accumulation of the synthesized NPs and enhance their stability, they were coated by hydrophilic polyethylene glycol (PEG) with a molecular weight of 3450 Da. In this design, maleic anhydride was as a carboxyl source. Briefly, 0.13 g maleic anhydride and 3.6 g PEG were dissolved in 10 ml dry toluene for 8 h at 80 °C under stirring. Then, yielded PEG diacid was precipitated into hexane for three times and dried by oven. Next, dopamine was used as a linker. For this purpose, 517 mg PEG diacid was dissolved in a solution of $CHCl_3$ (15 ml) and DMF (10 ml) consisting of N-Hydroxysuccinimide, N-ethyl-N (3-dimethyl aminopropyl), Carbodiimide hydrochloride (NHS/EDC), anhydrous Na_2CO_3 (100 mg), and dopamine hydrochloride (10.27 mg). The solution was mechanically stirred at room temperature for 2 h. Thereafter, the solution of NPs was slowly added after sonication for about 15 min under N_2. After 24 h, the modified NPs were precipitated by adding hexane, separated by magnet, and dried under N_2. Then, NPs were dissolved in deionized water and dialyzed through a 12 kDa bag for 24 h in water.

In order to functionalize the synthesized NPs with D-glucosamine, 10 ml of coated NPs (1 mM) was added to the solution of EDC (0.5 mM)/NHS (0.25 mM) and stirred for 30 min at room temperature. 10 ml D-glucosamine, with the final concentration of 2 mg/ml, was added to 20 ml of the above solution, and the resulting mixture was stirred at room temperature for 2 h and then purified by dialysis bag (Scheme 1) [32, 43].

2.3 Characterization of Fe₃O₄-PEG-DG

To investigate the physicochemical properties of Fe_3O_4-PEG-DG NPs, X-ray diffraction (XRD) was applied to study the Fe_3O_4 nuclei before and after the addition of PEG and DG, dynamic light scattering (DLS) was used to determine the particle size distribution and surface zeta potential of the prepared NPs, vibrating-sample magnetometer (VSM) was done for investigating the magnetism of the NPs, field emission scanning electron microscopy (FE-SEM) was utilized for analysing the morphology of NPs, Fourier transform infrared spectroscopy (FTIR) was performed to investigate the binding of PEG and DG to Fe_3O_4 NPs.

2.4 In vitro MRI

To investigate the effect of Fe_3O_4-PEG-DG NPs on reducing MRI signal intensity, T2 relaxation time test was done by 1.5 Tesla clinical MRI device at different concentrations of Fe (0.1, 0.25, 0.5, 0.75, and 1 mM). Samples of different concentrations were prepared in 1 ml microtubes which were

submerged in water in a rack. Distilled water was used as control sample.

T2 relaxation time calculations were performed using Standard Spin Echo, # of Echoes = 32, TE = 13, 26, 39, 52, 66, 79, 92, 105, 118, 145, 158, 171, 184, 198, 211, 237, 250, 264, 277, 290, 330, 343, 356, 369, 382, 396, and 422 (ms), TR = 20, 50, 100, 200, 400, 2000, and 3000 (ms), matrix = 256*256, Slice Thickness = 1/5 (mm), FOV = 18*18 (cm), NEX = Non protocol. Further analysis was performed using Dicomwork (version 1.3.0.5), Microdicom (version 0.7.1.1824), and MATLAB (version 1.0.0.1). The results were plotted as a signal intensity diagram vs. TE values for different Fe concentrations.

2.5 Cytotoxicity Analysis of Fe₃O₄-PEG-DG NPs on Normal Human Kidney (HEK-293) Cell Line by MTT Assay

The HEK-293 cell line was delivered in flasks from the Pasteur Institute of Iran (Tehran, Iran). After incubation of CO_2-incubated cells for two days, the cells were passaged in two 75 ml flasks. To do so, the previous culture flask was discarded, and the cells were washed with PBS. By adding 5 ml trypsin, cells were isolated from the flask surface by incubation for 5 min at 37 °C. The remaining cells were completely separated by pipetting, and after adding 10 ml of FBS-containing culture medium to neutralize trypsin, cells were transferred into 15 ml falcon encompassing 4 ml RPMI cell culture medium containing 10% FBS. Then after, 1% PBS was added and thoroughly mixed. 2 ml of cell suspension and 8 ml of culture medium were poured into two 75 ml flasks which were placed in a CO_2 incubator after mixing. In each flask, the cells were incubated for 72 h in a solution containing Fe_3O_4-PEG-DG NPs at different concentrations. After 72 h, the cell culture medium was removed, and MTT reagent was added at a concentration of 5 mg/ml. After a while the soluble purple formazan crystals formed. The MTT solution was then removed from the wells, and DMSO solution was added to dissolve formazan precipitants. The optical density plate was then mounted on an ELISA device and measured at a wavelength of 570 nm [44, 45].

2.6 Investigating the biodistribution of Fe₃O₄-PEG-DG NPs in animal model using SPECT

All animal studies were performed based on animal rights. To investigate the biodistribution of Fe_3O_4-PEG-DG NPs in the animal model, rats and CT/SPECT model (Siemens, simbia T2) equipped with LEHR collimators were used. To label the NPs with di-glucose amine, 0.1 ml of $SnCl_2$ solution (4 mg/ml) and 370 99mTco4 MBq in 2 ml isotonic saline, obtained from 99Mo/99mTc generator, to a kit

A

B

HOOC-PEG-COOH

C

DPA-PEG-COOH

D

Fe₃O₄-DPA-PEG-COOH

E
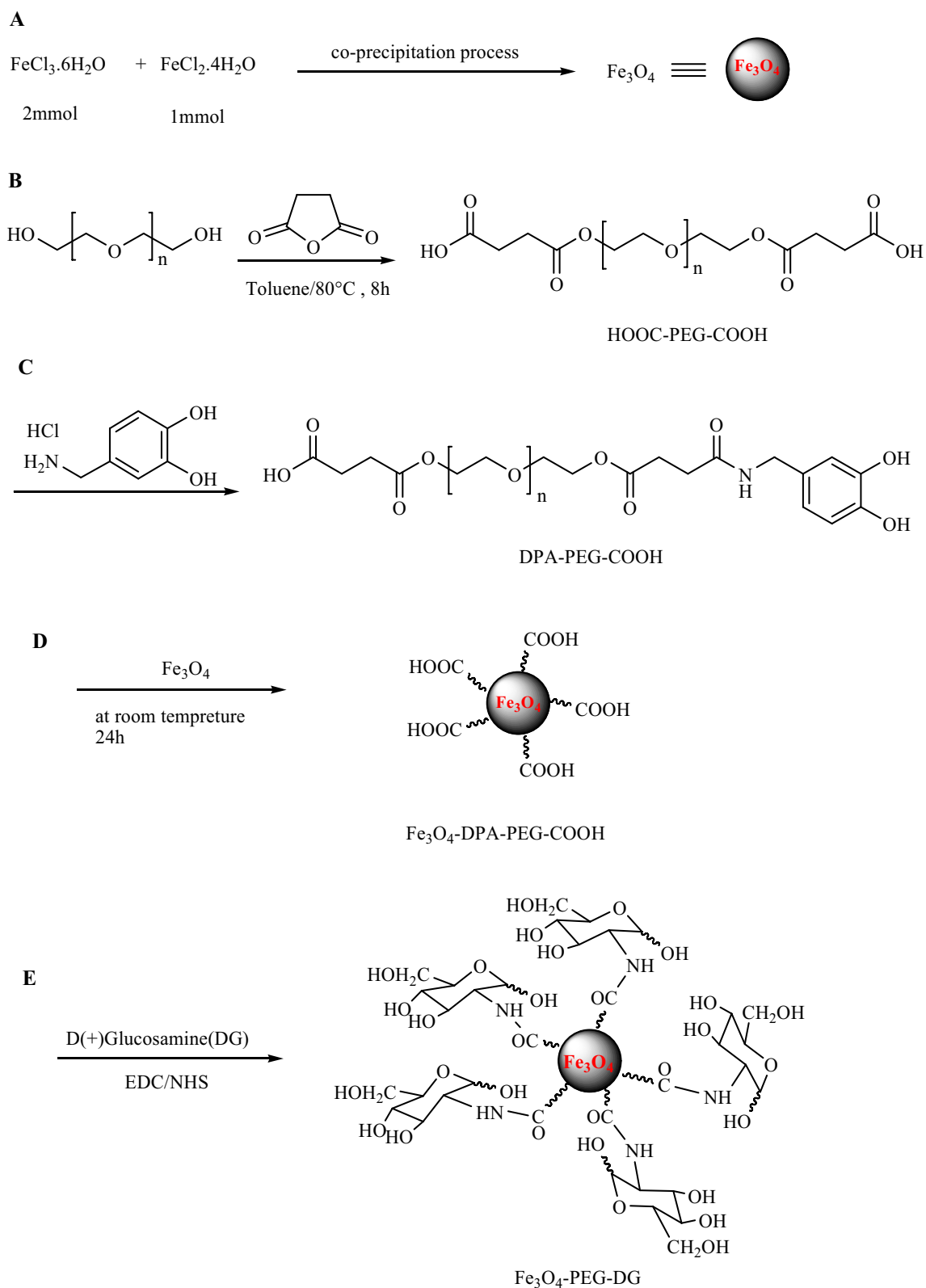
Fe₃O₄-PEG-DG

Scheme 1 Synthesis of Fe₃O₄-PEG-DG

containing 1 mg of smart nanoparticles. It is added with glucosamine and incubated at room temperature for 20 min. Then, NPs labelled with technetium 99 were injected into the animal through the tail vein, and SPECT images were taken immediately 40 min post-injection.

3 Results and discussion

3.1 XRD analysis

Figure 1a shows the XRD pattern of the synthesized Fe_3O_4 NPs. By comparing the obtained pattern with the reference, the type of the synthesized iron oxide, i.e., Fe_2O_3 or Fe_3O_4, can be determined. As seen, the peak that has the highest intensity is related to (311) planes ($2\theta = 35.5°$). Also, the second and third peaks (in terms of intensity) are at different 2θ angles for each material. Regarding magnitude, the second peak corresponds to (440) planes ($2\theta = 62.5°$), and the third peak is related to (220) planes ($2\theta = 30.5°$); whereas, the location of hematite is supplanted. Also, the expansion at the peaks of XRD patterns is related to the size of the crystals, and as the size decreases, the peak expansion increases [46]. As a result, the type of the synthesized iron oxide NPs is determined to be Fe_3O_4 [47, 48]. Characteristic peaks of the synthesized Fe_3O_4 NPs completely match with the reference (JCDPS-19–0629) [49] proving that Fe_3O_4 NPs have been successfully synthesized.

Size calculations of the synthesized NPs are carried out using the Scherrer method (Eq. 1)

$$d = \frac{K\lambda}{B\cos\theta_0} \tag{1}$$

where K is a dimensionless shape factor which has a value between 0.8 and 1 (in most cases is considered $K \approx 0.9$), λ is the x-ray wavelength, B is the physical width of a reflection (in 2θ), and θ_0 is the Bragg angle of a line maximum [50]. The obtained particle size using the Scherrer equation is 18 nm.

3.2 DLS analysis

The size and size distribution of NPs are strongly dependent on the synthesis method [51]. For instance, in the co-precipitation method, the particle size distribution is non-uniform and can affect the properties and thus the application of NPs. In general, the more uniform the particle size distribution, the more homogeneous the properties of NPs. One of the crucial synthesis parameters is pH of the solution during the formation of Fe_3O_4 NPs' nuclei which is usually between 9 and 14 resulting in a finer particle as the pH rises. In this study, Fe_3O_4 NPs were synthesized at pH 12 which led to synthesis of small NPs, as the average size of NPs without and with PEG coating is 23.3 and 47.2 nm, respectively. This difference in size is associated with the presence of

Fig. 1 **a** X-ray diffraction of synthesized NP, **b** Comparison of X-ray diffraction of synthesized NP with reference (JCDPS-19–0629)
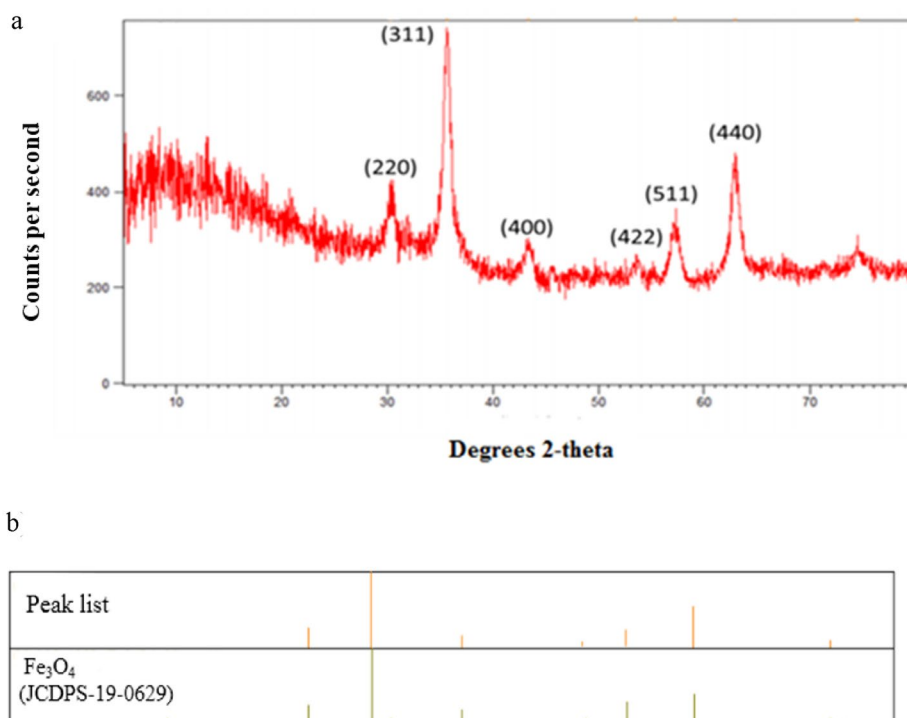
PEG [52]. Also, the average size of Fe_3O_4-PEG-DG NPs is determined 98 nm.

Moreover, to ascertain the surface charge of Fe_3O_4-PEG-DG NPs, zeta potential analysis was done. Due to the ubiquity of a carboxyl group on the surface of NPs, the surface charge should be negative (equal to -19.72 ± 0.32 mV), yet zeta potential of Fe_3O_4-PEG-DG NPs has become more positive (equal to -7.15 ± 0.14 mV). This decrease in surface charge could be due to the binding of glucose amine to carboxylic groups leading to dropping the number of carboxylic groups on the surface of Fe_3O_4-PEG-DG NPs.

3.3 FTIR Analysis

Figure 2a shows the FTIR spectrum of pure Fe_3O_4 NPs in which the characteristic peak at 578.96 cm^{-1} represents the stretching vibration of Fe–O bond. Thereafter carboxylation of polyethylene glycol, in the polymer chain the OH groups are reinstated by the COOH. To be prepared for FTIR analysis, the polymer goes under precipitation by hexane and is dried in oven. As shown in Fig. 2b, the peak at 1729 cm^{-1} is related to the C=O bond of COOH indicating the successful carboxylation of the polyethylene glycol [38, 53, 54].

For Fe_3O_4-PEG NPs (Fig. 2c), the absorption peak at 1625 cm^{-1} is ascribed to the stretching vibration of acidic C=O confirming the presence of acidic groups on the surface of Fe_3O_4-PEG NPs. By comparing the FTIR spectra of PEG diacid and Fe_3O_4-PEG NPs at the wavelength of 1625 cm^{-1}, it could be observed that the resulted peak has been broadened. This can be due to presence of dopamine aromatic ring. Moreover, the peaks at 1104 and 2874 cm^{-1} are due to C–O–C bond and asymmetric stretching of C–H bond of Fe_3O_4-PEG NPs, respectively. These results completely consist with the obtained results by Feng et al. [53]. Also, the peak observed at 1465 cm^{-1} is due to bending vibrations of CH$_2$ group. Therefore, these FTIR spectra demonstrate that PEG-COOH has been successfully grafted onto the surface of Fe_3O_4 NPs.

Figure 2d depicts the FTIR spectrum of Fe_3O_4-PEG-DG NPs. As seen, the absorbent peak at 1108 cm^{-1} is due to the stretching vibration of C–N bond indicating the successful attachment of glucose amine. Moreover, the peaks at 1646 and 1553 cm^{-1} are attributed to O–H bond and stretching vibration of O-C-O bond, respectively. Also, the characteristic peak at 583 cm^{-1} is related to the stretching vibration of Fe–O bond [53, 54].

3.4 FE-SEM analysis

The morphology and particle size of Fe_3O_4-PEG and Fe_3O_4-PEG-DG NPs were studied using FE-SEM analysis
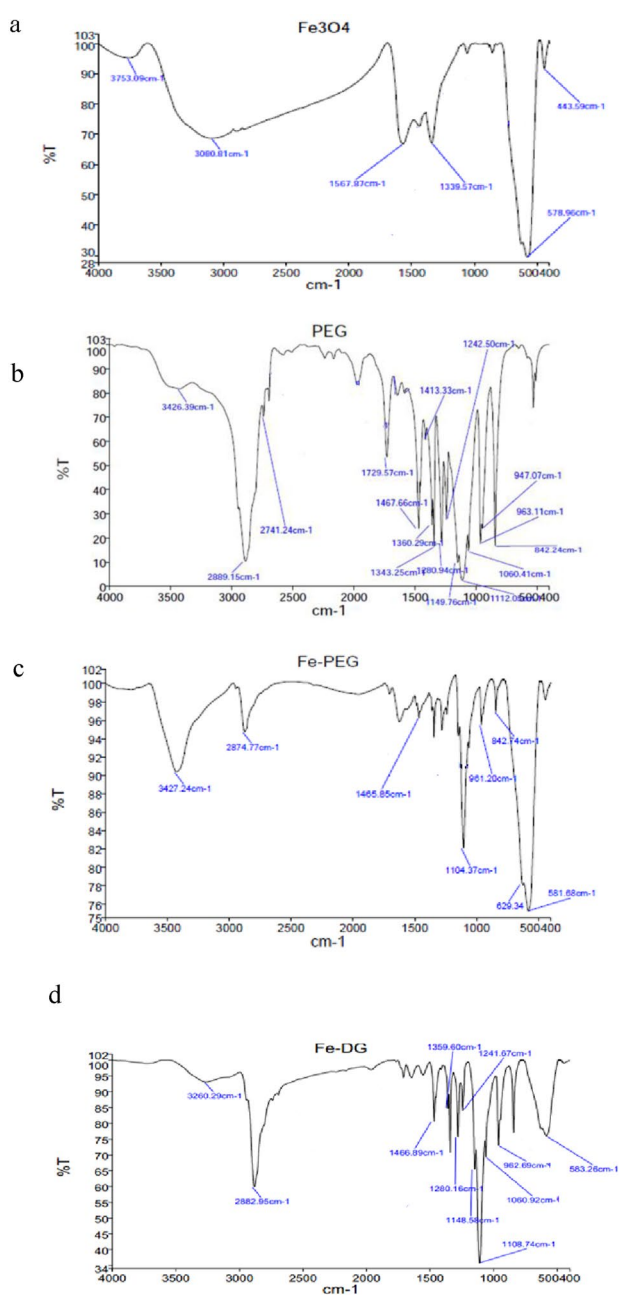

Fig. 2 FTIR spectra of **a** pure Fe_3O_4 NP, **b** PEG diacid, **c** Fe_3O_4 NPs coated with PEG diacid, and **d** D-glucose amine functionalized NPs

[55]. Since the hydrodynamic diameter of NPs is usually larger than their actual size detected by the electron microscope, for more accurate investigation and getting a high-resolution image of the prepared samples, FE-SEM was used. As seen in Fig. 3a, b, the size of Fe_3O_4-PEG and Fe_3O_4-PEG-DG NPs is smaller than 30 and 50 nm, respectively.
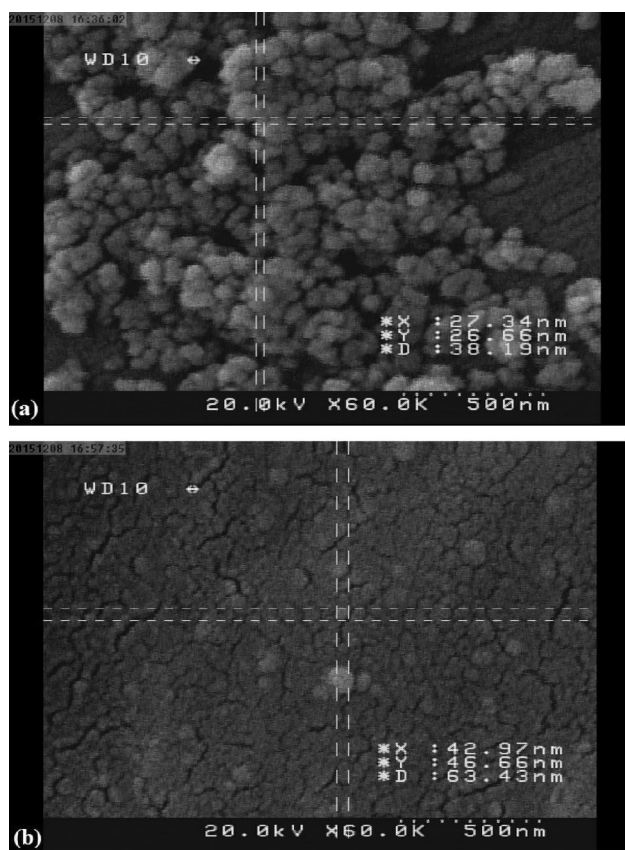
Fig. 3 The FE-SEM images of **a** Fe_3O_4-PEG and **b** Fe_3O_4-PEG-DG NPs

3.5 VSM analysis

Fe_3O_4 NPs have different magnetic properties according to their structure and size [56]. Figure 4 shows the obtained VSM graphs of the non-coated and coated Fe_3O_4 NPs. PEG has been used as a coating material owing to its good biocompatibility, nontoxicity, and biodegradability. It should be noted that the use of a non-magnetic material for coating may reduce the magnetic properties of Fe_3O_4 NPs [56]. As shown in Fig. 4b, the saturation magnetism of the prepared NPs has reduced from 56 emu/g to 30 emu/g after coating with PEG.

3.6 In vitro MRI Analysis

In order to evaluate Fe_3O_4-PEG-DG NPs as an MRI contrast agent, in vitro MRI analysis was carried out at different concentrations of the sample. As seen in the Fig. 5, the ability of Fe_3O_4-PEG-DG NPs to reduce the signal intensity and create a negative contrast increases, as the Fe concentration soars, so that the produced image is darkened incrementally.

As found from Table 1, Fe_3O_4-PEG-DG NPs have a significant effect on the reduction of signal intensity, as this

effect has increased with an increase in Fe concentration of the NPs. Synthetic magnetic NPs, with an effect on the T2 relaxation time of the proton, encompass NPs cause increase of the contrast and cause the darkening of the environment include NPs [38, 57].

It has been previously reported that size of a contrast agent could impact its ability to reduce signal intensity, as the smaller the particle size, the lower the T_2 relaxivity [38]. Also, as shown in Fig. 4, PEG coating has curtailed the magnetism of the NPs which could affect the magnetic property and thus the capability of the NPs to reduce the signal intensity.

3.7 Evaluation of Cell Toxicity

The cytotoxicity test was performed on normal human kidney (HEK-293) cells at different concentrations of the prepared samples and was repeated three times. According to the results, non-coated Fe_3O_4 NPs (200 μM), Fe_3O_4-PEG NPs (50 and 100 μM), and Fe_3O_4-PEG-DG NPs (50 and 100 μM) exhibited different biocompatibility features in 72 h of treatment.

The selection of HEK-293 cells was due to the fact that most of the contrast agents exhibit the highest toxicity on kidney, and kidney tissue is highly vulnerable against MRI contrast agents. As shown in Fig. 6, cell viability of HEK-293 treated with Fe_3O_4-PEG-DG NPs and Fe_3O_4-PEG NPs (50 and 100 μM) was more than 75% and these nanoparticles had a very slight toxicity. This is because coating Fe_3O_4 NPs with PEG reduces the cytotoxicity, especially for a kidney cell line [58]. Also, there is no meaningful difference between two concentrations of Fe_3O_4-PEG-DG NPs in terms of cytotoxicity indicating that a change (at this particular range) in their concentration does not alter their level of cytotoxicity noticeably. These results are consistent with a study by Amendola et al. (2021) on the toxicity of PEG-Ag-Fe NP [52].

The slight cytotoxicity of Fe_3O_4-PEG-DG NPs stems from different issues as follows: (1) Conjugation of DG to the NPs impedes its phosphorylation inside the cell, so it turns into an antimetabolite and thus demonstrates cytotoxicity. (2) DG exhibits an increased EPR effect and prolonged entrapment time inside the cell. (3) DG is internalized by the cell through transporter-mediated endocytosis leading to an intensified cellular uptake and thus enhanced cytotoxicity.

3.8 Investigating the Biological Distribution of Fe_3O_4-PEG-DG NPs in the Animal Model

Tc^{m99} labeled Fe_3O_4-PEG-DG NPs were injected through the tail vein of rats. Images taken at 0 and 40 min after injection show that Tc^{m99} labeled Fe_3O_4-PEG-DG NPs have entered the animal's digestive tract, which is well

Fig. 4 Magnetization curves of **a** pure Fe_3O_4 NPs and **b** Fe_3O_4-PEG NPs
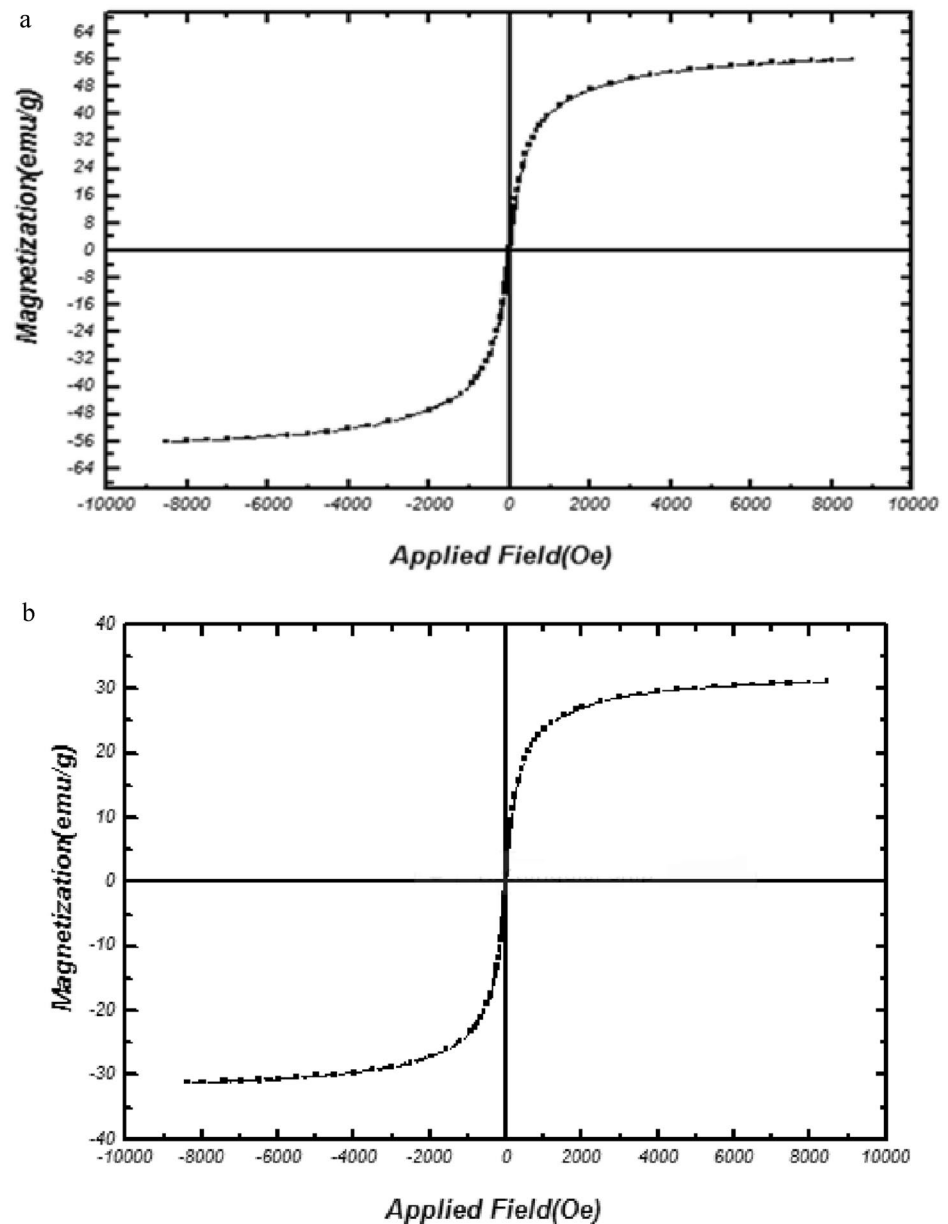
seen in the peritoneum, gastrointestinal tract, and visceral system. Especially at 40 min after injection, the injected NPs show an even distribution in the digestive tract which suggests that these NPs tend to be highly sensitive to tissues that have active metabolism, such as gastrointestinal tract. Glucose can be used for imaging of a variety of areas and tissues of the body, one of which is the gastrointestinal tract, and the obtained result completely justifies that Tc^{m99} labeled Fe_3O_4-PEG-DG NPs have entered the digestive tract. (**F**ig. 7)

4 Conclusion

In this study, Fe_3O_4-PEG-DG nanoparticles were synthesized to improve MRI images. The hydrodynamic sizes of NPs were 23 and 98 nm pre and post conjugation, respectively. XRD, VSM, FTIR and FESEM were used to characterize the nanoparticles. Fe_3O_4-PEG-DG nanoparticles compare to other contrast agent were not toxic to normal human kidney cell line of HEK-293. In vitro MRI analysis for Fe_3O_4-PEG-DG NPs showed significant decrement of signal intensity with an increment in Fe concentration.

Fig. 5 **a** T2 relaxation time curves and **b** MRI images of Fe_3O_4-PEG-DG NPs at different Fe concentrations
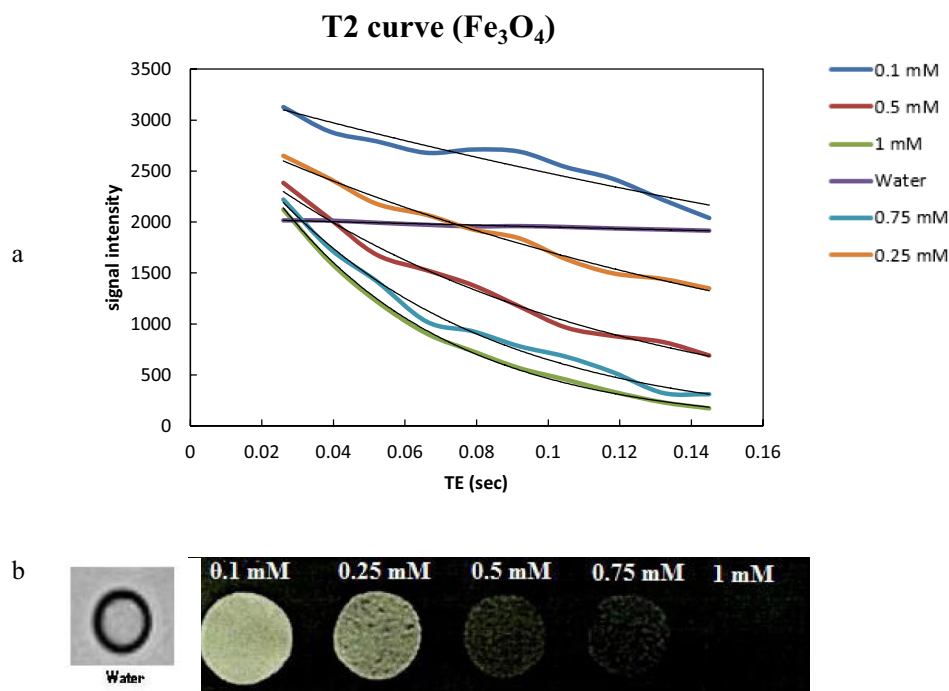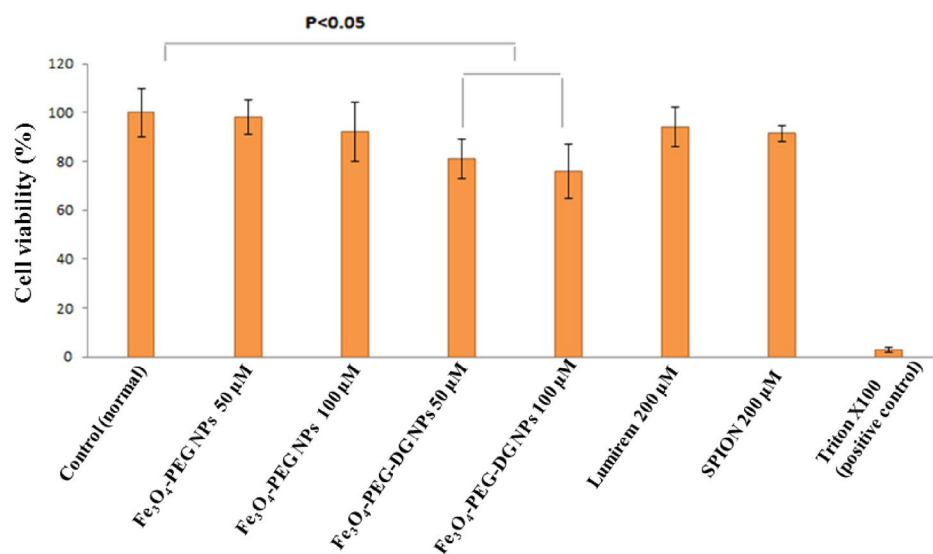

Table 1 T2 relaxation time for different Fe concentrations of Fe_3O_4-PEG-DG NPs

Fe concentration (mM)	Water	0.1	0.25	0.5	0.75	1
$1/T_2$ (s^{-1})	0.44	3.01	5.7	10.2	16.5	20.7
T_2 (s)	2.3	0.33	0.18	0.1	0.06	0.05

Fig. 6 Diagram of cell viability vs. different concentrations of Fe_3O_4, Fe_3O_4-PEG, Fe_3O_4-PEG-DG NPs, and Lumirem®

MRI images also revealed that Fe_3O_4 NPs reduced the T_2 relaxation time and increased the negative contrast effect. The results of the SPECT imaging showed that Tc^{m99} labeled NPs were well integrated into the gastrointestinal tract of the animal. Particularly, within 40 min after injection, the distribution of labeled NPs was clearly seen in the gastrointestinal tract. Due to the appropriate size of the prepared NPs, as well as adequate PEG coating, stability
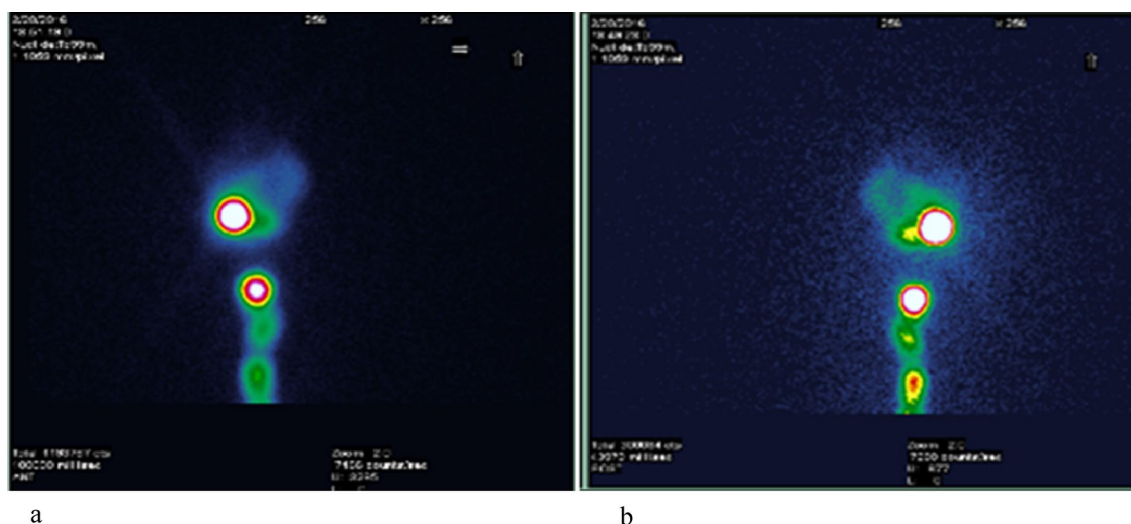
Fig. 7 From left to right, SPECT images of mice at 0 (**a**) and 40 min (**b**) after injection of Tc^{m99} labeled Fe_3O_4-PEG-DG NPs

and biocompatibility of NPs increased. These nanoparticles can bind to other macromolecules such as anticancer drugs and target drug release. These nanoparticles can be used as a multi-agent nanosystem for simultaneous therapeutic and diagnostic applications. For this reason, continuing research in this field is very important in medicine and can not only reduce costs but also bring patient satisfaction.

References

1. H.L. Karlsson, P. Cronholm, J. Gustafsson, L. Moller, Chem. Res. Toxicol. **21**(9), 1726–1732 (2008)
2. T.F. Massoud, S.S. Gambhir, Genes Dev. **17**(5), 545–580 (2003)
3. M. Shokeen, C.J. Anderson, Acc. Chem. Res. **42**(7), 832–841 (2009)
4. Y. Nitheesh, R. Pradhan, S. Hejmady, R. Taliyan, G. Singhvi, A. Alexander, P. Kesharwani, S.K. Dubey, Mater. Sci. Eng. **130**, 112441 (2021)
5. R. Weissleder, Science **312**(5777), 1168–1171 (2006)
6. H.R. Herschman, Science **302**(5645), 605–608 (2003)
7. M.A. Pysz, S.S. Gambhir, J.K. Willmann, Clin. Radiol. **65**(7), 500–516 (2010)
8. M. Mahmoudi, V. Serpooshan, S. Laurent, Nanoscale **3**(8), 3007–3026 (2011)
9. S.S. Gambhir, Nat. Rev. Cancer **2**(9), 683 (2002)
10. L.W. Dobrucki, A.J. Sinusas, Nat. Rev. Cardiol. **7**(1), 38 (2010)
11. W. Cheng, Y. Ping, Y. Zhang, K.-H. Chuang, Y. Liu, Journal of healthcare engineering. **4**(1), 23–46 (2013)
12. K. Brindle, Nat. Rev. Cancer. **8**(2), 94 (2008)
13. R. Weissleder, M.J. Pittet, Nature **452**, 580 (2008)
14. M.E. Phelps, J. Nucl. Med. **41**(4), 661–681 (2000)
15. A.M. Wu, P.J. Yazaki, S.-W. Tsai, K. Nguyen, A.-L. Anderson, D.W. McCarthy, M.J. Welch, J.E. Shively, L.E. Williams, A.A. Raubitschek, Proc. Natl. Acad. Sci. **97**(15), 8495–8500 (2000)
16. X. Chen, Y. Hou, M. Tohme, R. Park, V. Khankaldyyan, I. Gonzales-Gomez, J.R. Bading, W.E. Laug, P.S. Conti, J. Nucl. Med. **45**(10), 1776–1783 (2004)
17. A. Fatima, M. Ahmad, A.K.A. Al saidi, A. Choudhury, Y. Chang, G.H. Lee, Nanomaterials **11**(9), 2449 (2021)
18. F. Xiong, K. Hu, H. Yu, L. Zhou, L. Song, Y. Zhang, X. Shan, J. Liu, N. Gu, Pharm. Res. **34**(8), 1683–1692 (2017)
19. T. Hemalatha, P. Prabu, D.N. Gunadharini, M.K. Gowthaman, Int. J. Biol. Macromol. **112**, 250–257 (2018)
20. N. Gholipour, M. Akhlaghi, A. Mokhtari kheirabadi, P. Geramifar, D. Beiki, Int. J. Biol. Macromol. **148**, 932–941 (2020)
21. H. Yang, Y. Miao, L. Chen, Z. Li, R. Yang, X. Xu, Z. Liu, L.-M. Zhang, X. Jiang, Int. J. Biol. Macromol. **148**, 483–492 (2020)
22. D.S. Wilbur, Bioconjug. Chem. **3**(6), 433–470 (1992)
23. W. Lin, T. Hyeon, G.M. Lanza, M. Zhang, T.J. Meade, MRS Bull. **34**(6), 441–448 (2009)
24. A.J.L. Villaraza, A. Bumb, M.W. Brechbiel, Chem. Rev. **110**(5), 2921–2959 (2010)
25. P.V. Prasad, *Magnetic resonance imaging: methods and biologic applications*, vol. 124 (Springer Science & Business Media, Berlin, 2006)
26. M. Babincova, D. Leszczynska, P. Sourivong, P. Babinec, Med. Hypotheses **54**(2), 177–179 (2000)
27. P. Moroz, S. Jones, B. Gray, Int. J. Hyperth. **18**(4), 267–284 (2002)
28. P. Caravan, J.J. Ellison, T.J. McMurry, R.B. Lauffer, Chem. Rev. **99**(9), 2293–2352 (1999)
29. A.K. Gupta, M. Gupta, Biomaterials **26**(18), 3995–4021 (2005)
30. M. Mahmoudi, A. Simchi, M. Imani, A.S. Milani, P. Stroeve, J. Phys. Chem. B **112**(46), 14470–14481 (2008)
31. J. Xie, C. Xu, Z. Xu, Y. Hou, K.L. Young, S. Wang, N. Pourmand, S. Sun, Chem. Mater. **18**(23), 5401–5403 (2006)
32. J. Xie, C. Xu, N. Kohler, Y. Hou, S. Sun, Adv. Mater. **19**(20), 3163–3166 (2007)

33. D. Liu, J. Li, C. Wang, L. An, J. Lin, Q. Tian, S. Yang, Nanomedicine. **32**, 102335 (2021)
34. B. Wu, K. Deng, S.-T. Lu, C.-J. Zhang, Y.-W. Ao, H. Wang, H. Mei, C.-X. Wang, H. Xu, B. Hu, Biomaterials. **268**, 120531 (2021)
35. A.K. Iyer, G. Khaled, J. Fang, H. Maeda, Drug Discov. Today **11**(17–18), 812–818 (2006)
36. M.V. Liberti, J.W. Locasale, Trends Biochem. Sci. **41**(3), 211–218 (2016)
37. C. Barron, E. Tsiani, T. Tsakiridis, Expression of the glucose transporters GLUT1, GLUT3, GLUT4 and GLUT12 in human cancer cells. BMC proc. **6**(3), 1 (2012)
38. A.H. Rezayan, M. Mousavi, S. Kheirjou, G. Amoabediny, M.S. Ardestani, J. Mohammadnejad, J. Magn. Magn. Mater. **420**, 210–217 (2016)
39. J. Malakootikhah, A.H. Rezayan, B. Negahdari, S. Nasseri, H. Rastegar, Carbohyd. Polym. **170**, 190–197 (2017)
40. M. Shakourian-Fard, A.H. Rezayan, S. Kheirjou, A. Bayat, M.M. Hashemi, Bull. Chem. Soc. Jpn. **87**, 982–987 (2014)
41. R.A. Taheri, A.H. Rezayan, F. Rahimi, J. Mohammadnejad, M. Kamali, Biosens. Bioelectron. **86**, 484–488 (2016)
42. F. Oroojalian, A.H. Rezayan, W.T. Shier, K. Abnous, M. Ramezani, Int. J. Pharm. **523**(1), 102–120 (2017)
43. N.C. Joshi, A. Gaur, A. Singh, J. Inorg. Organomet. Polym Mater. **30**, 4416–4425 (2020)
44. X. Ling, R. Jarubula, J. Inorg. Organomet Polym. Mater. **31**(3), 1373–1380 (2021)
45. H. Alvandi, A. Hatamian-Zarmi, B.E. Hosseinzadeh, Z.B. Mokhtari-Hosseini, E. Langer, H. Aghajani, Carbohydr. Polym. Technol. Appl. **2**, 100159 (2021)
46. M. Bououdina, T. Alwqyan, L. Khezami, B. Al-Najar, M. Shaikh, R. Gill, A. Modwi, K.K. Taha, O. Lemine, J. Alloy. Compd. **772**, 1030–1039 (2019)
47. M. Ghorbaanee, A.A. Salarian, V. Saba, J. Inorg. Organomet. Polym. Mater. **28**(5), 2169–2178 (2018)
48. A. Aarthi, M. Umadevi, R. Parimaladevi, G.V. Sathe, S. Arumugam, P. Sivaprakash, J. Inorg. Organomet. Polym. Mater. **31**(4), 1469–1479 (2021)
49. Y. Todaka, M. Nakamura, S. Hattori, K. Tsuchiya, M. Umemoto, Mater. Trans. **44**(2), 277–284 (2003)
50. G. Dorofeev, A. Streletskii, I. Povstugar, A. Protasov, E. Elsukov, Colloid J. **74**(6), 675–685 (2012)
51. H. Mohammadi, E. Nekobahr, J. Akhtari, M. Saeedi, J. Akbari, F. Fathi, Toxicol. Rep. **8**, 331–336 (2021)
52. V. Amendola, A. Guadagnini, S. Agnoli, D. Badocco, P. Pastore, G. Fracasso, M. Gerosa, F. Vurro, A. Busato, P. Marzola, J. Colloid Interface Sci. **596**, 332–341 (2021)
53. B. Feng, R.Y. Hong, L.S. Wang, L. Guo, H.Z. Li, J. Ding, Y. Zheng, D.G. Wei, Colloids Surf. A Physicochem. Eng. Asp. **328**(1), 52–59 (2018)
54. E. Kalantari, M.A. Khalilzadeh, D. Zareyee, J. Inorg. Organomet. Polym. Mater. **31**(1), 319–330 (2021)
55. R.M. Abdallah, R.M.S. Al-Haddad, J. Inorg. Organomet. Polym. Mater. **32**, 478–485 (2022)
56. S. Kumar, R.R. Singh, P.B. Barman, J. Inorg. Organomet. Polym. Mater. **31**(2), 528–541 (2021)
57. A. Ebrahimpour, N.R. Alam, P. Abdolmaleki, B. Hajipour-Verdom, F. Tirgar, T. Ebrahimi, M. Khoobi, J. Inorg. Organomet. Polym. Mater. **31**(3), 1208–1216 (2021)
58. J.V. Jokerst, T. Lobovkina, R.N. Zare, S.S. Gambhir, Nanomedicine **6**(4), 715–728 (2011)